

Mani-GS: Gaussian Splatting Manipulation with Triangular Mesh

Xiangjun Gao^{1*}, Xiangyu Li^{2*}, Yiyu Zhuang³, Qi Zhang², Wenbo Hu²,
Chaopeng Zhang^{2 †}, Yao Yao^{3 †}, Shan Ying², and Long Quan¹

¹ The Hong Kong University of Science and Technology

² Tencent AI Lab

³ Nanjing University

https://gaoxiangjun.github.io/mani_gs/

Abstract. Neural 3D representations such as Neural Radiance Fields (NeRF), excel at producing photo-realistic rendering results but lack the flexibility for manipulation and editing which is crucial for content creation. Previous works have attempted to address this issue by deforming a NeRF in canonical space or manipulating the radiance field based on an explicit mesh. However, manipulating NeRF is not highly controllable and requires a long training and inference time. With the emergence of 3D Gaussian Splatting (3DGS), extremely high-fidelity novel view synthesis can be achieved using an explicit point-based 3D representation with much faster training and rendering speed. However, there is still a lack of effective means to manipulate 3DGS freely while maintaining rendering quality. In this work, we aim to tackle the challenge of achieving manipulable photo-realistic rendering. We propose to utilize a triangular mesh to manipulate 3DGS directly with self-adaptation. This approach reduces the need to design various algorithms for different types of Gaussian manipulation. By utilizing a triangle shape-aware Gaussian binding and adapting method, we can achieve 3DGS manipulation and preserve high-fidelity rendering after manipulation. Our approach is capable of handling large deformations, local manipulations, and soft body simulations while keeping high-quality rendering. Furthermore, we demonstrate that our method is also effective with inaccurate meshes extracted from 3DGS. Experiments conducted demonstrate the effectiveness of our method and its superiority over baseline approaches.

Keywords: Gaussian Splatting · Manipulation · Rendering

1 Introduction

Manipulating and editing 3D content is essential for content creation and has various applications in movies, gaming, and virtual/augmented reality. 3D model editing enables users to create and modify models flexibly, thereby enhancing production efficiency. The traditional pipeline for modeling and editing a 3D asset with photo-realistic rendering involves a process with geometry modeling,

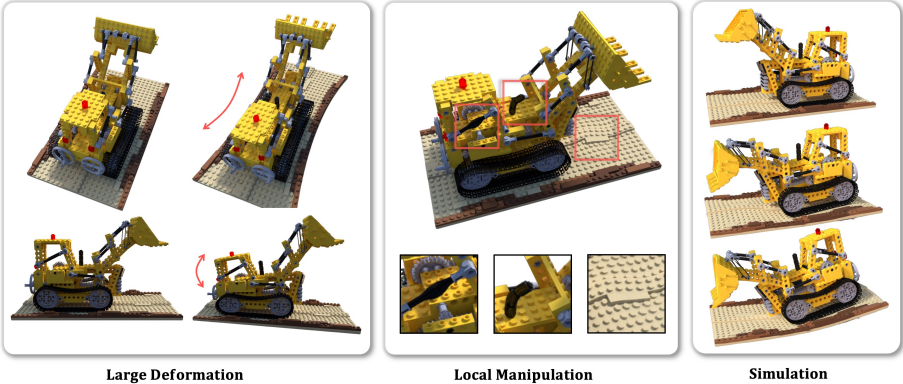


Fig. 1: Our proposed approach allows for 3DGS manipulation, including *large deformation*, *local manipulation*, and even *physical simulation* (such as soft body simulation), while maintaining high-quality rendering. Please zoom in for more details.

texturing, UV mapping, lighting, and rendering, which is a tedious and time-consuming flow requiring lots of manual work.

Over the past few years, the neural radiance field (NeRF) [21] has been widely studied due to its high capability and simple reconstruction process in 3D representation. However, the implicit representation poses challenges for editing. To address this, some methods are proposed to edit this implicit neural radiance field [21]. NeRF-Editing [43] is the first to utilize the triangular mesh to help edit the implicit radiance field. They train a canonical NeuS [31] and extract the triangular mesh from NeuS [31]. A tetrahedra grid is then constructed to contain the object mesh. To render the deformed object by editing the triangular mesh, a volume rendering is conducted in the deformed space. The sampling points in deformed space are mapped to canonical space based on the constructed tetrahedra grid, where the points in deformed space have the same tetrahedron barycentric coordinate in the same tetrahedron with their corresponding points in canonical space. Moreover, [10, 18] demonstrate similar ideas by employing tetrahedra to deform sampling points and achieve editable nerf-based scenes. Instead, Neu-Mesh [38] and SERF [47] define the neural radiance field by associating each mesh vertex with radiance and geometry features. Then they can conduct volume rendering like Point-NeRF [36] in deformed space without backward mapping. However, these editing methods based on implicit neural radiance fields still suffer from inconvenient manipulation, suboptimal rendering results, and long training and rendering times.

Meanwhile, 3DGS [14] has gained significant attention in differential rendering due to its high-fidelity and fast rendering proficiency. However, despite being an explicit 3D representation, it still lacks an effective method for manipulating 3DGS while maintaining high-quality rendering. SuGaR [7], the work most closely related to our objective, develops a novel algorithm to extract a trian-

gular mesh from 3DGS. Although their main goal is not to facilitate editable photorealistic rendering, they bind the 3DGS to the extracted mesh, enabling model animation as demonstrated in their demo.

This work proposes a method that enables 3DGS manipulation, achieving high-quality and photo-realistic rendering. Our key insight is to manipulate 3DGS using a triangular mesh as the proxy, which allows for direct transfer of mesh manipulation to 3DGS with 3DGS self-adaptation. With our methods, we can achieve *large deformation*, *local manipulation*, and *soft body simulation* with high-quality results as shown in Figure 1, which also avoid the need to design various algorithms for different types of manipulation.

To achieve controllable 3DGS manipulation through the mesh, an intuitive approach is to bind the GS to lay perfectly on the triangle and enforce the GS to be thin enough. After mesh manipulation, the GS will automatically adapt its rotation and position with the attached triangle, as employed in SuGaR [7]. However, SuGaR heavily relies on the accuracy of mesh geometry, inheriting the defects of mesh rendering. Specifically, for inaccurate parts, SuGaR cannot inpaint the missing parts or remove the redundant parts in the final rendering.

Adding an offset to the position of attached Gaussians during the reconstruction may seem like a reasonable solution to compensate for mesh inaccuracy. However, this fixed offset cannot be generalized well to the deformed space after novel manipulation. Our proposed solution is to define a local coordinate system for each triangle, which we refer to as *local triangle space*. We then bind Gaussians to each triangle and optimize the Gaussian attributes, including rotation, position, and scaling, in the attached *local triangle space*.

During mesh manipulation, the attributes in the local triangle space remain unchanged, while the global Gaussian position, scaling, and rotation will be self-adaptively adjusted according to our proposed formula. As a result, our proposed approach enables us to manipulate 3DGS using a triangular mesh while maintaining rendering quality. Since our Gaussians are set to be free outside the triangle, we can also support high-fidelity manipulation even when the Gaussians are bound to an inaccurate mesh, exhibiting a high tolerance for mesh accuracy.

GaMeS [6] and Mesh-GS [28] are two concurrent works that also employ triangular meshes for Gaussian Splatting manipulation. In particular, GaMeS [6] constrains the Gaussians on the surface exactly; Mesh-GS [28] permits an offset along the normal direction without adapting the Gaussian scale when the triangle shape changes. In contrast, our model allows for Gaussian move in the triangle local space which means we can achieve high-quality rendering without the need for accurate mesh. Gaussian scaling also adapts in response to changes in triangle shape when large deformations are applied to the mesh.

In summary, the contributions of our paper are listed as follows:

- We propose a 3DGS manipulation method that can effectively transfer the triangular mesh manipulation to 3DGS and maintain high-quality rendering.
- We introduce a triangle shape aware Gaussian binding strategy with self-adaption, which has a high tolerance for mesh accuracy and supports various 3DGS manipulations.

- We evaluate our method and achieve state-of-the-art results, demonstrating various 3DGS manipulations, including *large deformation*, *local manipulation*, and *soft body simulation*.

2 Related Work

2.1 NeRF Editing

Recently, neural radiance field [21] (NeRF) has garnered significant attention due to its high-quality and photo-realistic rendering results for novel view synthesis. NeRF represents the scene as a continuous function that maps a spatial location and viewing direction to a volume density and color, which is parameterized by a multilayer perceptron (MLP). Owing to the implicit representation that encodes the scene within the network parameters, editing and deforming the geometry of the NeRF scene explicitly like mesh can be challenging. To enable user editing of NeRF, [19] introduce editing conditional radiance fields trained on a shape category. However, it only supports basic editing operations, such as removing/adding object parts or shape transfer. CLIP-NeRF [29] achieves NeRF editing with text or images by leveraging CLIP model [23] but still can not edit the geometry locally. Some other work [1, 32, 34, 44] edit the NeRF in texture level which is not the focus of this paper.

To edit and deform NeRF locally, [10, 18, 43] construct a tetrahedra grid based on the underlying 3D shape. After explicitly deforming the tetrahedra into the posed space for editing, the sampled 3D points are mapped from the posed space to the canonical space through the unaltered tetrahedron, which means the canonical position can be calculated from the shared barycentric coordinate for both deformed and canonical tetrahedron. The density and radiance in the posed space can be calculated for the mapped sampling points in canonical space. On the other hand, [30, 38, 47] employ mesh as the guidance for deformation. NeuMesh [38] presents a novel representation to encode neural implicit field on a mesh-based scaffold for geometry and texture editing. [30] achieves the manipulation of both the geometry and color of neural implicit fields through differentiable colored meshes. Furthermore, there are several methods [2, 20, 25, 45, 46] that particularly focus on editing NeRF for avatar. In this work, we introduce an editing method based on 3DGS for general objects.

2.2 Mesh-based NeRF Rendering

NeRFs have shown impressive rendering results, however, rendering one pixel using NeRF representation necessitates a volumetric rendering algorithm that involves inferring MLP hundreds of times to estimate their radiance and density. This process is significantly slower than traditional mesh rendering. To accelerate NeRF rendering, several methods [3, 3, 24, 27, 40, 41] have been proposed to combine NeRF representation with mesh reconstruction. By converting this implicit representation to an explicit mesh, these methods may also facilitate applications like editing. In particular, MobileNeRF [3] represents NeRF as a collection

of polygons with deep feature textures, which can be rendered using the classic polygon rasterization pipeline, generating a feature vector for each pixel and passing it to an MLP to decode the color. MobileNeRF is capable of achieving rendering even on standard mobile devices. Additionally, NeRFMeshing [24] distills the reconstructed NeRF into a signed surface approximation network to extract 3D mesh and shows the simulation results for editing. BakedSDF [41] proposes a neural surface-volume representation to extract the mesh and supports editing like material decomposition, appearance editing, and physics simulation. However, the editing results of these methods heavily rely on the accuracy of the extracted mesh. Artifacts present in the mesh will directly influence the editing results. In contrast, our method demonstrates robustness to the reconstructed mesh and can still yield promising results even with the inaccurate mesh.

2.3 Gaussian Splatting Editing, Simulation and Animation

3D Gaussian Splatting [14] presents an innovative 3D Gaussian scene representation, accompanied by a differentiable renderer that attains real-time rendering of radiance fields while maintaining high quality. Initially, 3D Gaussian Splatting focuses solely on static scenes, which has been extended to model dynamic scenes [9, 17, 33, 39, 48], human avatars [8, 15, 22, 37, 42, 49], Gaussian Splatting simulation and animation [4, 7, 12, 35]. Specifically, SuGaR [7] proposes a method to extract meshes from 3D Gaussian Splatting with additional regularization, in which they bind 3DGS on extracted mesh and animated with Gaussian Splatting rendering. GSP [4] incorporates physically-based fluid dynamics in 3DGS and PhysGaussian [35] introduces a unified simulation-rendering pipeline that generates physics-based dynamics with photorealistic renderings. VR-GS [12] achieves interactive physics-based editing in Virtual Reality. In this work, we also introduce a Gaussian Splatting manipulation method that binds Gaussian Splatting to the mesh, achieving state-of-the-art results.

3 Method

Recently, due to its exceptional high-fidelity rendering capabilities and fast rendering speed, Gaussian Splatting [14] has emerged as a popular 3D representation in the differential rendering field. However, despite being an explicit 3D representation, it still lacks a methodology for manipulating this 3D representation for editing while maintaining high-quality rendering after the manipulation. In this work, giving multi-view RGB images of an object as input, we introduce a method for object manipulation that can achieve photorealistic editable rendering by employing Gaussian Splatting.

The pipeline of our method is illustrated in Figure 2 and consists of three main stages. First, we extract a mesh from 3D Gaussian Splatting (3DGS) or a neural surface field for subsequent 3D Gaussian binding (Sec. 3.2). Next, we devise a novel Mesh-Gaussian binding method dedicated to manipulating Gaussian Splatting while maintaining photo-realistic rendering quality (Sec. 3.3). Finally,

we describe the types of Gaussian manipulation we support and how to render the manipulated results (Sec. 3.4).

3.1 Preliminary

Thanks to its superior capability for high-fidelity and rapid rendering, 3D Gaussian Splatting (3DGS) [14] has recently emerged as a popular 3D representation in differential rendering. 3DGS utilizes explicit 3D Gaussians as its primary rendering primitives. A 3D Gaussian point is mathematically defined as:

$$G(\mathbf{x}) = \exp\left(-\frac{1}{2}(\mathbf{x} - \boldsymbol{\mu})^\top \Sigma^{-1}(\mathbf{x} - \boldsymbol{\mu})\right). \quad (1)$$

Each 3D Gaussian point is characterized by a 3D mean position coordinate $\boldsymbol{\mu}$ and a covariance matrix Σ . Additionally, each Gaussian has an opacity \boldsymbol{o} and a view-dependent color \mathbf{c} represented by a set of spherical harmonics (SH). To ensure that the covariance matrix Σ retains its meaningful interpretation, it is parameterized as a unit quaternion \mathbf{q} and a 3D scaling vector \mathbf{s} , defined as $\Sigma = \mathbf{R}\mathbf{S}\mathbf{S}^\top\mathbf{R}^\top$.

To render an image from a specific viewpoint, 3D Gaussians are projected onto the image plane, resulting in 2D Gaussians. The 2D covariance matrix is approximated as:

$$\Sigma' = \mathbf{J}\mathbf{W}\Sigma\mathbf{W}^\top\mathbf{J}^\top, \quad (2)$$

where \mathbf{W} and \mathbf{J} denote the viewing transformation and the Jacobian of the affine approximation of perspective projection transformation [50], respectively. The 2D means are calculated through the projection matrix. After this, the pixel color is composited through the alpha blending of N ordered 2D Gaussians:

$$\mathcal{C} = \sum_{i \in N} T_i \alpha_i \mathbf{c}_i \quad \text{with} \quad T_i = \prod_{j=1}^{i-1} (1 - \alpha_j). \quad (3)$$

Here, α is obtained by multiplying the opacity \boldsymbol{o} with the 2D covariance’s probability computed from Σ' and pixel coordinate on the image space.

3.2 Mesh Extraction

Our method is capable of achieving high-quality reconstruction and editing using guided meshes obtained from various methods. In this section, we investigate different mesh extraction and reconstruction techniques with different mesh accuracy and processing time to guide the 3D Gaussians in our approach.

Screened Poisson Reconstruction. 3D Gaussian Splatting could be considered a type of point cloud, making it intuitive to extract the mesh using the Poisson-reconstruction algorithm. However, the 3D Gaussians do not have normal vectors for reconstruction. Inspired by recent 3DGS inverse rendering

methods [5, 16], we allocate an additional gaussian attribute, normal \mathbf{n} , for 3D Gaussians:

$$\{\mathcal{D}, \mathcal{N}\} = \sum_{i \in N} T_i \alpha_i \{d_i, \mathbf{n}_i\}, \quad (4)$$

where d_i denotes the depth and \mathbf{n}_i denotes the normal of each gaussian point. To optimize the normal, we then encourage the rendered normal \mathcal{N} to be well-aligned with the pseudo-normal map $\hat{\mathcal{N}}$, computed from the rendered depth \mathcal{D} based the local planarity assumption. After training 3DGS with normal attributes, we can extract the mesh using the Screened poisson surface reconstruction [13] algorithm.

Marching Cube for Gaussian Splatting. In DreamGaussian [26], the method attempts to summarize the alpha values of neighboring Gaussian points as the composite density value of marching cube sampling points. The Gaussian points within a pre-defined local voxel are considered neighbors. However, We found that this method often ignores the thin and small structures. To address this issue, we employ ball query Nearest Neighbor searching methods to search only the nearest Gaussian points of grid sampling points. The sampling points that have a neighbor within a pre-defined distance are assigned with a density value of 1, otherwise with a density value of 0. The geometry is then extracted using the Marching Cube. This approach allows for the extraction of thin and small structures, even though they may be slightly larger than the actual surface. With our Mesh-Gaussian binding strategy, we can achieve high-fidelity rendering with the slightly inaccurate mesh and support smooth Gaussian manipulation.

Neural Implicit Surfaces. In this work, we also try to extract high-quality surfaces from the implicit representation utilizing the method proposed in NeuS [31]. NeuS suggests extracting a surface as the zero-level set of a signed distance function (SDF), which has consistently served as a robust and widely used benchmark in the realm of neural surface reconstruction. Nevertheless, the surface derived from NeuS may encompass an excessive number of triangle surfaces, which may have around 1.5 million. A large number of triangles can negatively affect both training and inference speeds, therefore, we employ a mesh cleaning process to eliminate the noisy floaters and utilize mesh decimation techniques to reduce the count of triangles to approximately 300K. We circumvent the need for such a high number of triangles while maintaining high-fidelity rendering.

3.3 Binding Gaussian Splatting on Mesh

Owing to the exceptional proficiency in high-fidelity and fast rendering, 3DGS has gained significant attention in differential rendering. However, despite being an explicit 3D representation, it currently lacks a method for effectively manipulating 3DGS while preserving high-quality rendering simultaneously. Mesh editing techniques, such as large-scale deformation, localized manipulation, and simulation, have been widely acknowledged and extensively researched for many years. Our primary objective is to associate the 3DGS with mesh triangles,

enabling the manipulation of 3DGS and its rendering results following mesh editing.

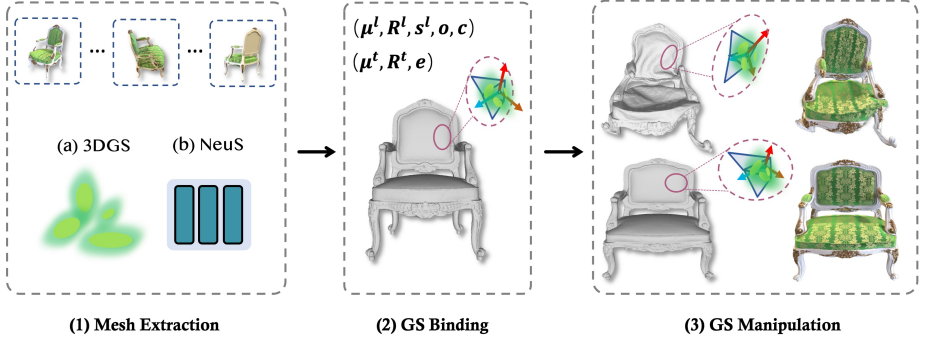


Fig. 2: Overview of our method. (1) Firstly, we extract a triangular mesh from 3DGS [14] or a neural surface field (NeuS [31]). (2) Next, we bind N Gaussians to each triangle in the local triangle space, and optimize the local Gaussian attributes (μ^l, R^l, s^l, o, c) . The triangle attributes (μ^t, R^t, e) are calculated based on the triangle vertices. (3) Finally, we manipulate 3DGS by transferring the mesh manipulation directly, thus achieving manipulable rendering.

Given a reconstructed or extracted triangular mesh \mathbf{T} with K vertices $\{\mathbf{v}_i\}_{i=1}^K$ and M triangles $\{\mathbf{f}_i\}_{i=1}^M$, the goal of our method is to construct a 3DGS model bound to mesh triangles and optimize each Gaussian attribute $\{\mu_i, \mathbf{q}_i, \mathbf{s}_i, o_i, \mathbf{c}_i\}$. To simplify the notation, we will omit the subscript in subsequent sections.

For each triangle \mathbf{f} in the given mesh \mathbf{T} , which is composed of three vertices $(\mathbf{v}_1, \mathbf{v}_2, \mathbf{v}_3)$, we initialize N Gaussians on this triangle. To be specific, the mean position μ of initialized Gaussians is formulated as $\mu = (w_1 \mathbf{v}_1 + w_2 \mathbf{v}_2 + w_3 \mathbf{v}_3)$, $\mathbf{w} = (w_1, w_2, w_3)$ is the pre-defined barycentric coordinate of each Gaussians attached on the triangle. And \mathbf{w} satisfy $(w_1 + w_2 + w_3) = 1$.

Gaussians on Mesh. To achieve controllable 3DGS manipulation through the mesh, an intuitive way is to perfectly attach the GS to the triangle, as shown in the SuGaR [7]. With the rotation matrix denoted as $\mathbf{R} = \{\mathbf{r}_1, \mathbf{r}_2, \mathbf{r}_3\}$ and the scaling vector represented by $\mathbf{s} = (s_1, s_2, s_3)$, SuGaR train 3DGS with a flat Gaussian distribution on the mesh by setting $s_1 = \epsilon$, where ϵ is close to zero. \mathbf{r}_1 is defined by the normal vector \mathbf{n} of the attached triangle. The Gaussians have only 2 learnable scaling factors (s_2, s_3) instead of 3, and only 1 learnable 2D rotation rather than a quaternion, to keep the Gaussians flat and aligned with the mesh triangles. This type of binding strategy heavily relies on mesh accuracy, which lacks the flexibility of 3DGS to model complex object rendering. Moreover, the mesh quality obtained from SuGaR is significantly inferior compared to the ground truth and recent neural surface reconstruction results, which increases the difficulty of editing.

Gaussians on Mesh with Offset. To compensate for the inaccuracy of the extracted mesh, it would be better to add an offset $\Delta\mu$ to the Gaussians 3D mean

μ , which enables the Gaussians to move out of the attached triangle f . Although it could improve the rendering quality of the reconstructed static object, it would result in noisy and unexpected rendering distortion in the manipulated object due to the mismatched localized relative position between Gaussians.

Triangle Shape Aware Gaussian Binding and Adapting. To preserve the high-fidelity rendering results after manipulation, the key lies in maintaining the local rigidity and preserving the relative location between Gaussians, both for 3D means and rotations. Our key insight is to define a local coordinate system in each triangle space.

The first axis direction of triangle space is defined as the direction of the first edge. The second axis direction of triangle space is defined as the triangle’s normal direction. The third axis direction of triangle space is defined as the cross product of the first and second axis. Then the triangle coordinate system rotation can be formulated as:

$$\mathbf{R}^t = [r_1^t, r_2^t, r_3^t] = \left[\frac{(\mathbf{v}_2 - \mathbf{v}_1)}{\|\mathbf{v}_2 - \mathbf{v}_1\|}, \mathbf{n}^t, \frac{(\mathbf{v}_2 - \mathbf{v}_1)}{\|\mathbf{v}_2 - \mathbf{v}_1\|} \times \mathbf{n}^t \right] \quad (5)$$

where $\mathbf{v}_1, \mathbf{v}_2$ is the first and second vertex location respectively, \mathbf{n}^t is the normal vector which can be calculated by:

$$\mathbf{n}^t = \frac{(\mathbf{v}_2 - \mathbf{v}_1) \times (\mathbf{v}_3 - \mathbf{v}_1)}{\|(\mathbf{v}_2 - \mathbf{v}_1) \times (\mathbf{v}_3 - \mathbf{v}_1)\|}. \quad (6)$$

We then optimize the Gaussians’ local position μ^l and local rotation \mathbf{R}^l in triangle space instead of the global position and rotation in the original 3DGS.

Then the global rotation, scale and location of 3DGS are as follows:

$$\mathbf{R} = \mathbf{R}^t \mathbf{R}^l, \mathbf{s} = s^l, \quad \mu = \mathbf{R}^t \mu^l + \mu^t \quad (7)$$

where, μ^t is the global coordinate of each triangle center. In practice, we initialize N local Gaussian points and bind them for each Gaussian point, whose initialized position is on the triangle uniformly.

This Gaussian mesh binding method can preserve the relative position and rotation between Gaussians that are bonded on neighboring triangles after mesh manipulation. However, following mesh manipulation, not only does the triangle center change but also the triangle shape. With the altered triangle shape, the local Gaussian position and scaling should adjust accordingly. When the triangle enlarges, it is intuitive that the local scaling and position should expand as well:

$$\mathbf{R} = \mathbf{R}^t \mathbf{R}^l, \mathbf{s} = \beta \mathbf{e} s^l, \quad \mu = \mathbf{e} \mathbf{R}^t \mu^l + \mu^t, \quad (8)$$

where β is a hyper-parameter, *adaption vector* $\mathbf{e} = [e_1, e_2, e_3]$ is designed to make sure that the global scaling \mathbf{s} is proportionable to the triangle shape. The first axis is along the first edge, so e_1 is designed as the length l_1 of the first edge of the triangle. The second axis is along the normal direction, we set $e_2 = (0.5 * (e_1 + e_3))$. The third axis is perpendicular to the first edge, we set e_3 as the average length of the second and third edges $(0.5 * (l_2 + l_3))$.

3.4 Manipulate Gaussian Splatting through Mesh

Utilizing our triangle shape aware gaussian binding and adapting strategy, upon the completion of model training and mesh manipulation, the 3DGS is instantly manipulated and adapted. During mesh manipulation, the attributes in the local triangle space remain unchanged. The triangle rotation, position, and edge length can be calculated instantly. Therefore, the global Gaussian position, scaling, and rotation can be self-adaptively adjusted following our proposed formula. In this paper, we exhibit the 3DGS manipulation rendering outcomes, such as large-scale deformation, local manipulation, and soft-body simulation, which are driven by the manipulated mesh. Many 3D design software applications possess the capability to execute mesh manipulation. In our experiments, we employ Blender to manipulate the mesh.

4 Experiments

4.1 Training Details

The first stage of our methods includes a mesh extracting stage, during which we extract triangular mesh from neural implicit surface field (NeuS [31]) or 3D Gaussian splatting (Screened Poisson or Marching Cube) only. However, the extracted mesh always contains enormous triangles, which we try to decimate to approximately 300K.

With the extracted mesh, we conduct the *triangle shape aware Gaussian binding and adapting* strategy on the mesh. For each triangle, we bind $N = 3$ Gaussian on the surface initially. The Gaussian attributes are optimized subsequently with the supervision of multi-view rendering loss in the second stage. We train our model for 30K iterations in the initial stage to extract mesh and 20K iterations in the second stage. All experiments are conducted on a single NVIDIA A100 GPU. Please see the supplementary material for more details.

4.2 Datasets, Metrics and Methods for Comparison

To evaluate our methods, we compare Mani-GS with previous editable novel view synthesis methods, a NeRF-based editing method NeRF-Editing [19] and a 3DGS-based editing method SuGaR [7]. For the evaluation, we employ the commonly used metrics: *PSNR*, *SSIM*, *LPIPS*. We evaluate our methods mainly on the NeRF Synthetic dataset [21] and DTU dataset [11].

4.3 Evaluation

Static Rendering Table 1 provides a quantitative comparison of all NeRF Synthetic 8 cases between our method and competing methods. We conducted experiments using their official code repository.

The numerical results of the NeRF-Editing were not presented in their original paper, we ran their code to provide more visual and numerical comparisons.

Table 1: Quantitative comparison of our methods with NeRF-Editing (*N.E.*) [19] and *SuGaR* [7] on NeRF Synthetic dataset in terms of SSIM, PSNR, LPIPS. (\uparrow means higher is better, \downarrow means lower is better.) The best results are marked in bold.

Subject	PSNR \uparrow			SSIM \uparrow			LPIPS \downarrow		
	<i>N.E.</i>	<i>SuGaR</i>	Ours	<i>N.E.</i>	<i>SuGaR</i>	Ours	<i>N.E.</i>	<i>SuGaR</i>	Ours
Chair	28.15	31.33	35.38	0.943	0.977	0.986	0.061	0.027	0.011
Drums	21.14	25.36	26.19	0.884	0.939	0.953	0.12	0.062	0.039
Ficus	23.82	29.94	35.40	0.909	0.959	0.986	0.104	0.039	0.013
Hotdog	32.67	35.45	37.49	0.969	0.980	0.984	0.048	0.035	0.019
Lego	29.16	32.09	36.33	0.944	0.968	0.982	0.074	0.037	0.015
Material	29.48	28.7	29.91	0.944	0.937	0.956	0.063	0.076	0.046
Mic	29.60	34.07	37.46	0.952	0.980	0.992	0.046	0.029	0.007
Ship	25.01	27.90	31.01	0.083	0.885	0.890	0.194	0.127	0.097
Average	-	30.61	33.65	-	0.9531	0.966	-	0.054	0.030

As depicted in Table 1, we observed some outliers in "*Drums, Ficus*" that were lower than even 10 PSNR compared to ours and *SuGaR*. Therefore, we remove these outliers with a strikethrough in the table. As can be observed, our approach surpasses all the baseline methods with respect to PSNR, SSIM, LPIPS, which means we achieve the best rendering quality. We are 3.0 higher than *SuGaR* in PSNR, 0.013 higher in SSIM, and 0.024 lower in LPIPS.

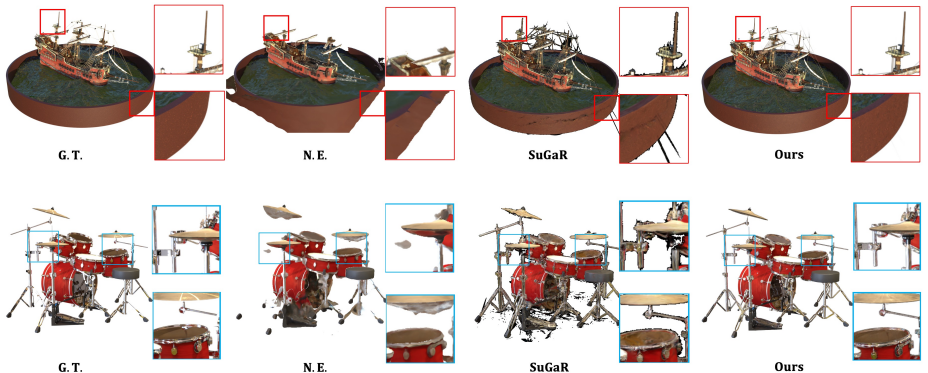


Fig. 3: Visual comparison between ours, NeRF-Editing [19](N.E.) and *SuGaR* [7] for static rendering. It illustrates our proposed method can contain a much more accurate boundary in "*Ship*" (first row), and detailed results in "*Drums*" (second row).

In Figure 3, we present qualitative results of our approach and other methods in overview and zoom-in details. Our methods render more detailed and more accurate boundaries. For *SuGaR*, it attempts to bind 3D Gaussians on the triangle and enforce that the attached Gaussian is closely aligned on the triangle. In practice, they set the scale s_1 along the triangle's normal direction to a value close to zero, i.e., $s_1 = \epsilon$. This binding strategy heavily depends on the accuracy of the mesh. As can be observed in the third column of Figure 3, wrong geometry leads to an inaccurate rendering, especially in the boundary region.

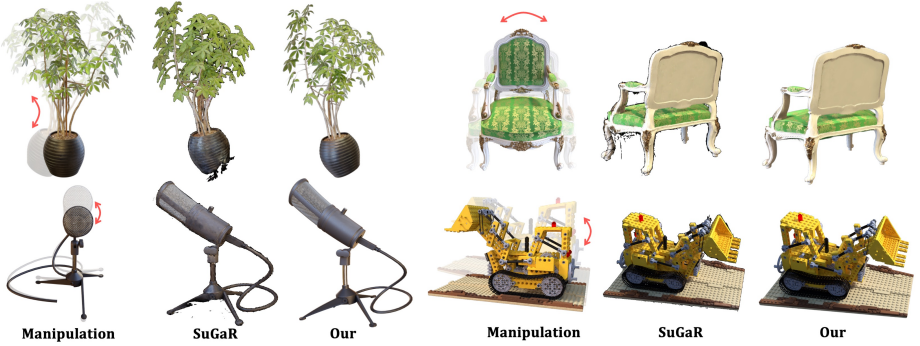


Fig. 4: We provide a visual comparison of manipulation rendering between our proposed approach and *SuGaR*. Our approach exhibits fewer artifacts and less blurring effect compared to *SuGaR*. For more details, please zoom in.

Manipulation Rendering In Figure 4, we showcase our manipulation results. In these four cases, we manipulate the underlying mesh with large deformation, the *Chair* is stretched, *Lego* is tapered, *Ficus* and *Mic* is bent to left and up respectively. As demonstrated in *Chair*, *Ficus*, we have more accurate boundary and shape, as well as in the bottom region. This indicates that when the geometry is not that accurate, *SuGaR* can not adapt to compensate for geometry error, which results in missing geometry and dilated boundary geometry. For *Lego*, *Mic*, we can maintain the high rendering quality even after the large deformation, while *SuGaR* shows some distortion and noise in rendering results after large deformation. We did not present the manipulation results of NeRF-Editing [19] since we did not obtain their relatively reasonable results in these cases.

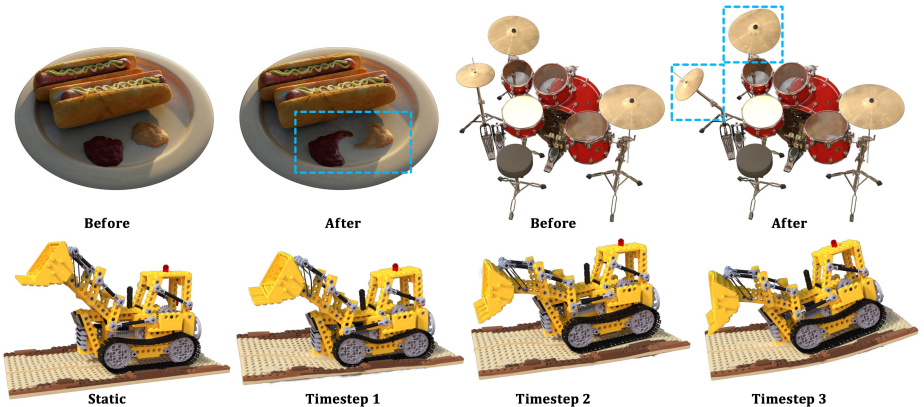


Fig. 5: Visual results of *local manipulation* and *soft body simulation*. In row 1, we demonstrate that our proposed GS-mesh binding method enables us to support local part manipulation, such as *blending*, *reposing*, and *elastic deformation*. In row 2, we showcase a 3DGS soft body simulation demo at different timesteps.

In addition to the large deformation, our method also produces promising results for local manipulation and physics simulation. Here we show an exam-

ple of soft body simulation. In Figure 5 row 1, we try to *blend* the red sauce and yellow sauce of *Hotdog* as shown in the blue box, which shows satisfying editing and reasonable rendering quality. In *Drums*, we *repose* a cymbal and *elastically deform* a cymbal as shown in the blue box. After reposing and elastic deformation, we still preserve the photo-realistic rendering results. Note that the manipulation is achieved by manipulating the triangular mesh directly, the 3DGS rendering is achieved simultaneously with self-adaption.

In the second row of Figure 5, we present the rendering results of soft body simulation at different timesteps. As observed, we can achieve 3DGS soft body simulation by just transferring the mesh simulation to 3DGS, which eliminates the need for a soft body simulation algorithm dedicated to 3DGS.

Table 2: Quantitative ablation comparison between *3DGS On NeuS Mesh*, *NeuS Mesh + Offset*, *Ours with Marching Cube Mesh*, *Ours with Screened Poisson Mesh* on NeRF Synthetic dataset. (\uparrow means higher is better, \downarrow means lower is better.)

Method	PSNR \uparrow	SSIM \uparrow	LPIPS \downarrow
3DGS On NeuS Mesh	30.87	0.9521	0.0447
NeuS Mesh + Offset	32.48	0.9625	0.0341
Ours + Marching Cube Mesh	32.11	0.9602	0.035
Ours + Screened Poisson Mesh	33.42	0.9638	0.0324
Ours + NeuS Mesh	33.45	0.9646	0.0309

4.4 Ablation Study

We conduct ablation studies to verify the effectiveness of triangle shape aware Gaussian binding and adapting method. We first evaluate the strategy of directly binding 3DGS to the mesh, which implies that the 3D position is fixed on the triangle. As shown in Table 2, the performance significantly drops, with a decrease of approximately 2.6 PSNR compared to our best model. For visual ablation in Figure 6, *3DGS on NeuS Mesh* after deformation shows a boundary with many burrs.

Next, we verify the effectiveness of adding 3D offset for 3DGS on Mesh. Although the offset can enhance the fitting of 3DGS to the static scene, as demonstrated in Table 2, it fails to generate satisfactory deformation rendering results because the offset only fits the static scene and remains unchanged during subsequent deformations. Consequently, it leads to significant noise and distortion after manipulation in Table 2.

Finally, we conduct experiments with different meshes extracted using different methods. The 3DGS Marching Cube Mesh (**3DGS MC**) is of low quality, including a dilated boundary and very noisy surface, as can be observed in Figure 6 row 2. The screened poisson mesh (**Poisson Recon.**) has some unconnected regions and missing parts compared with NeuS mesh (**NeuS**). However, using our triangle shape aware Gaussian binding and adapting method can still achieve

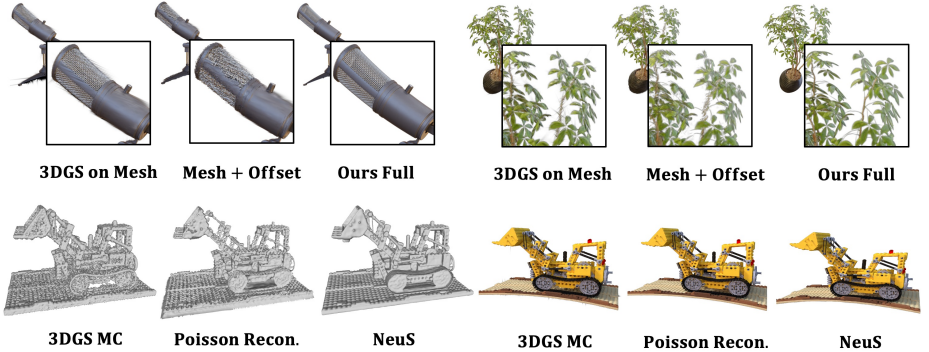


Fig. 6: Visual Results of Ablation Study. After deformation, (**3DGS on Mesh**) shows a burring boundary, (**Mesh + Offset**) leads to significant noise and distortion, (**Ours Full**) can maintain the high fidelity rendering. In the second row, we demonstrate that even with a low-quality mesh, we can still achieve high-quality editable rendering.

3DGS manipulation and maintain high-fidelity rendering even after very large deformation as shown in Figure 6 row 2. As shown in Table 2, the numerical results obtained with screened poisson mesh are only slightly lower than those obtained with NeuS mesh. When the mesh is of low quality, such as the **MC mesh**, the quantitative results are approximately 1 PSNR lower than the best, but still 2 PSNR higher than only binding 3DGS on the best Mesh (NeuS mesh), and 1.5 PSNR higher than SuGaR.

We also evaluate our method using mesh extracted from SuGaR, whose mesh is extremely dense. The PSNR using SuGaR mesh is 33.67, which is about 3 PSNR higher than that of the original SuGaR results.

5 Conclusion and Limitation

In this paper, we introduce a triangle shape aware Gaussian binding strategy with self-adaptation, which supports various 3DGS manipulations, maintains rendering quality, and has a high tolerance for mesh accuracy. We evaluate our methods on the NeRF synthetic dataset and demonstrate state-of-the-art results, showcasing various 3DGS manipulations, including large deformations, local manipulations, and soft body simulations.

During our experiments, we noticed that some results still exhibit distortions. When the local region of the manipulated mesh contains highly non-rigid deformations, it can result in rendering distortions. Additionally, during our simulation demos, we found that conducting physics simulations on meshes with more than 35K triangles can take hours. It would be a novel direction to explore fast simulation methods for 3DGS. Finally, we found that our results may not have accurate boundary rendering when the extracted mesh has a significant discrepancy from the ground truth mesh, such as unconnected regions.

Supplementary Material

In this supplementary material, we describe more implementation details of our method in Sec. A. Then, we give an efficiency analysis of training time and inference time in Sec. B. Besides, we also provide more visual rendering and geometry results on the NeRF [21] Synthetic dataset including some video demos in Sec. C. Finally, we further evaluate our methods on the DTU [11] dataset and provide qualitative and quantitative results in Sec. D.

A Implementation Details

A.1 Training Details of Mesh Extraction Stage

As outlined in our main paper, the first stage of our approach involves mesh extraction. While we utilize the NeuS [31] mesh as the foundation for binding Gaussians, we also explore extracting mesh from Gaussian-Splatting.

In this work, we try to extract triangular mesh using the Screened Poisson surface reconstruction [13] method from trained Gaussian-Splatting model. We incorporate a normal attribute \mathbf{n} for each 3D Gaussian and optimize the normal attribute with the pseudo-normal constraint.

The normal consistency is quantified as follows:

$$\mathcal{L}_n = \|\mathcal{N} - \tilde{\mathcal{N}}\|_2. \quad (9)$$

where \mathcal{N} is the rendered-normal map, $\tilde{\mathcal{N}}$ is the pseudo-normal map computed from rendered depth map.

Besides the normal constraint \mathcal{L}_n , the ordinary L1 Loss and Structural Similarity Index (SSIM) loss are also incorporated into optimization by comparing the rendered image \mathcal{C} with the observed image \mathcal{C}_{gt} . To address the issue of unwarranted 3D Gaussians in the background region, we employ a mask cross-entropy loss. This loss is defined as follows:

$$\mathcal{L}_{mask} = -B^m \log B - (1 - B^m) \log (1 - B), \quad (10)$$

where B^m denotes the object mask and B denotes the accumulated transmittance $B = \sum_{i \in N} T_i \alpha_i$.

Then all the loss terms can be summarized as follows:

$$\mathcal{L}_{stage1} = \lambda_1 \mathcal{L}_1 + \lambda_2 \mathcal{L}_{SSIM} + \lambda_3 \mathcal{L}_n + \lambda_4 \mathcal{L}_{mask}, \quad (11)$$

where $\lambda_1 = 1, \lambda_2 = 0.2, \lambda_3 = 0.01, \lambda_4 = 0.1$. We train this stage for 30K steps with adaptive density control, which is executed at every 500 iterations within the specified range from iteration 500 to 10K. Once the training stage is complete, we proceed with Screened Poisson surface reconstruction using the positions and normals of the Gaussians as input. The mesh extraction process takes less than 1 minute to complete.

In addition to mesh extraction, we also utilize Gaussian-Splatting Marching-Cube to extract the triangular mesh. Our approach involves sampling a grid with a resolution of $256 \times 256 \times 256$. For each sampling point, we identify its nearest Gaussian points. Sampling points that have the nearest Gaussians within a pre-defined distance threshold τ are assigned a density value of 1, while those that do not meet the threshold are assigned a density value of 0. τ is set to 0.01 in practice. The density threshold for Marching-Cube is set to $1e-4$.

Based on the visual comparison, the overall mesh quality can be ranked as follows: NeuS > Poisson Reconstruction > Marching-Cube.

A.2 Training Details of Gaussian-Binding Stage

To ensure an accurate representation of each triangle, we bind N Gaussians to it. Prior to training, we initialize the positions of the Gaussians on the attached triangle. The N initialized position is calculated using a barycentric coordinate, with a predefined barycentric coordinate set of $[1/2, 1/4, 1/4]$, $[1/4, 1/2, 1/4]$, $[1/4, 1/4, 1/2]$. For the hyper-parameter β mentioned in main paper equation (8), we set $\beta = 10$ in most cases, $\beta = 100$ in *Materials*.

In the Gaussian-Binding stage, we don't perform adaptive control because we find it doesn't influence the final performance. We also train 300K iterations in this stage with L1 loss, SSIM loss and mask entropy loss. The overall loss in this can be summarized as follows:

$$\mathcal{L}_{stage2} = \lambda_1 \mathcal{L}_1 + \lambda_2 \mathcal{L}_{SSIM} + \lambda_3 \mathcal{L}_{mask}, \quad (12)$$

where $\lambda_1 = 1, \lambda_2 = 0.2, \lambda_3 = 0.1$.

B Efficiency Analysis

The efficiency of GS Binding training and rendering speed depends on the number of Gaussians, which is the product of the triangle number T and the Gaussians number for each triangle N . In Table C, We first fixed T and tested different values of N . Our results indicate that $N=3$ leads to the best rendering quality while keeping a competitive rendering speed. When $N = 1$, the PSNR slightly decreased with a faster training and rendering speed.

We also evaluated the impact of underlying mesh resolution by testing meshes with different triangles (*270K, 150K, 70K*). As shown in Table C, the rendering quality decreases while efficiency improves with decreasing mesh resolution.

Regarding the editing time, it primarily depends on the time cost of mesh editing. We use Blender for mesh editing, and in our experience, *local manipulation* and *large deformation* can be achieved instantly. *Soft body simulation* can be a more time-consuming process, as it depends on the simulation algorithm employed in Blender.

Table C: Efficiency Analysis

	$N=4$	$N=3$	$N=1$	$N=1$	$N=1$
<i>Triangles(K)</i>	270	270	270	150	70
<i>Points(K)</i>	1080	810	270	150	70
<i>Training (min)</i>	16	13	7	5.5	4.5
<i>Speed (FPS)</i>	244	300	452	571	572
<i>PSNR</i>	36.36	36.39	36.27	35.86	34.52

C More Results on NeRF Synthetic Dataset

. **Soft Body Simulation.** In addition to the visual results presented in Figure 5 of the main paper, we also provide the geometry after simulation and rendering at different viewpoints in Figure G. To improve the speed of the mesh simulation, we decimated the original mesh from 300K to 35K triangles. While this may result in some decrease in rendering quality due to the reduced number of triangles as well as Gaussians, it was necessary to ensure reasonable simulation speed.

Demo Video. In order to further demonstrate the effectiveness of our methods, we have provided additional visual videos showcasing large deformation, soft body simulation, and local manipulation. These videos can be accessed through a local webpage by navigating to the *mani-gs* folder and clicking on *index.html*.

Numerical Comparison with NeuS and Neu-Mesh. We have compared our methods with NeuS and Neu-Mesh on the NeRF Synthetic dataset, and the results are presented in Table D. Our approach achieves a PSNR score that is 2.5 higher than Neu-Mesh, and a SSIM score that is 0.014 higher than Neu-Mesh, and a LPIPS score that is 0.012 lower than Neu-Mesh. These results demonstrate that our approach has achieved the best overall performance in all metrics compared to NeuS and Neu-Mesh on the NeRF Synthetic dataset.

Binding Gaussians on low-quality mesh. In some extreme cases, the Screened Poisson surface reconstruction method may result in a very low-quality triangular mesh. However, with our mesh-Gaussians binding strategy, we can still generate much better rendered images than those produced by *SuGaR* [7], even though *SuGaR* may have a much better mesh in such case as shown in Figure H.

D More Results on DTU Dataset

We have also evaluated our approach on the DTU dataset, which includes 15 cases with multi-view images as input. The results are presented in Table D, and demonstrate that our approach achieves a PSNR score that is 2.8 higher than Neu-Mesh, and a SSIM score that is 0.022 higher than Neu-Mesh. Additionally, our approach has a LPIPS score that is 0.016 lower than Neu-Mesh, indicating that our approach achieves the best overall performance on the DTU dataset.

We have also presented the manipulation results in Figure I. The left two columns showcase the geometry and rendered image before manipulation, while

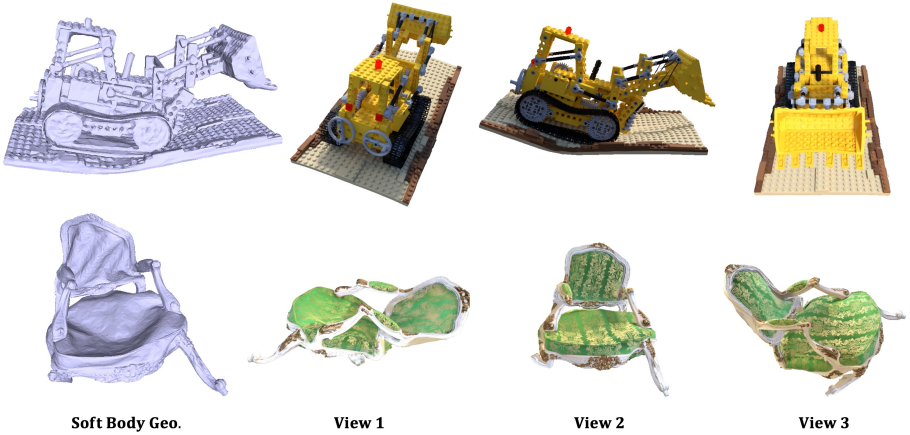


Fig. G: Visual results of softbody simulation at different viewpoints. The left column displays the geometry after simulation, while the right three columns showcase the rendering results from three different viewpoints.

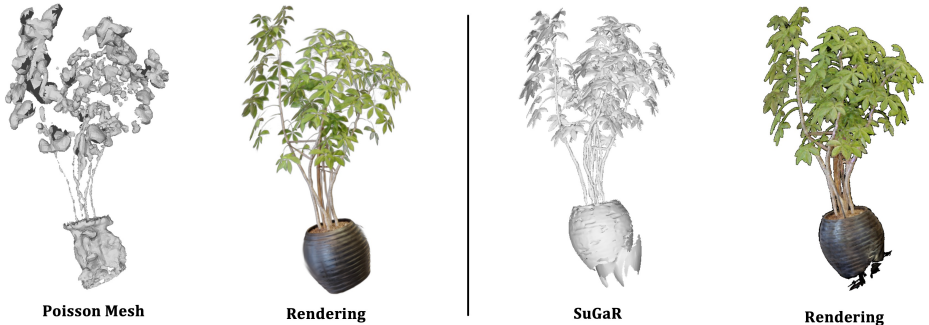


Fig. H: Binding Gaussians on a low-quality mesh (ours on the left, *SuGaR* on the right), we are still able to achieve high-fidelity manipulated rendering results when the mesh we generate of Screened Poisson reconstruction is of low quality. In contrast, *SuGaR* fails to produce satisfactory results, even though it has a better mesh in this particular case.

Methods	DTU			NeRF 360° Synthetic		
	PSNR \uparrow	SSIM \uparrow	LPIPS \downarrow	PSNR \uparrow	SSIM \uparrow	LPIPS \downarrow
NeuS [31]	26.352	0.909	0.176	30.588	0.960	0.058
Neu-Mesh [38]	28.289	0.921	0.117	30.95	0.951	0.043
Ours	31.496	0.943	0.088	33.45	0.965	0.031

Table D: We compare quantitative rendering quality with NeuS [31] and NeuMesh [38] on the DTU dataset and the NeRF Synthetic dataset.

the right three columns showcase the geometry and rendered image after manipulation. In the first row, the wing of a pigeon is manipulated, while in the second row, the arms of a tiger are swinging down. In the third row, a toy is twisted to the left. The manipulation results presented in Figure I demonstrate that our approach can successfully transfer mesh manipulation to Gaussian-Splatting, resulting in accurate and visually appealing results.

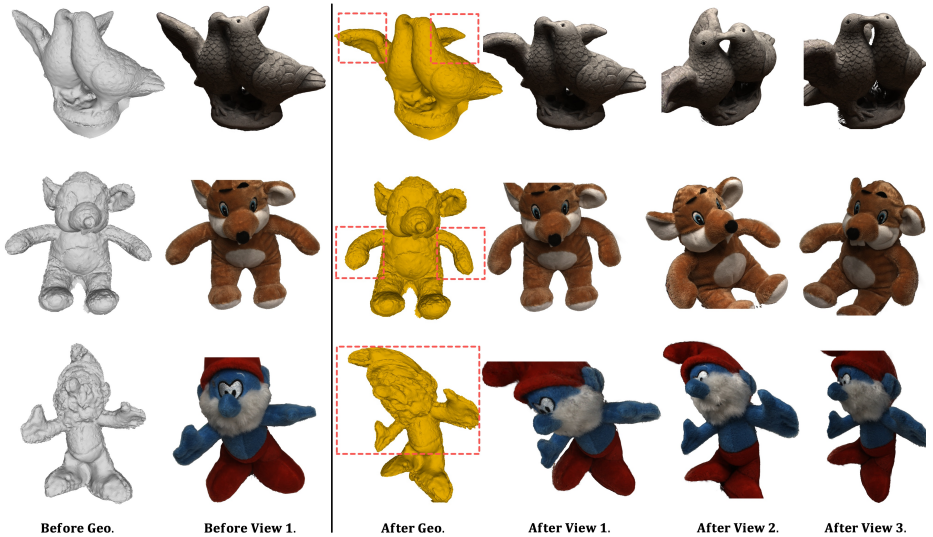


Fig. I: Manipulation rendering results in DTU dataset. The left two columns showcase the geometry and rendered image before manipulation, while the right three columns showcase the geometry and rendered image after manipulation. To highlight the deformed area, we have enclosed it within a red rectangle.

References

1. Bao, C., Zhang, Y., Yang, B., Fan, T., Yang, Z., Bao, H., Zhang, G., Cui, Z.: Sine: Semantic-driven image-based nerf editing with prior-guided editing field. In: Proceedings of the IEEE/CVF Conference on Computer Vision and Pattern Recognition. pp. 20919–20929 (2023) 4
2. Chen, Y., Wang, X., Chen, X., Zhang, Q., Li, X., Guo, Y., Wang, J., Wang, F.: Uv volumes for real-time rendering of editable free-view human performance. In: Proceedings of the IEEE/CVF Conference on Computer Vision and Pattern Recognition. pp. 16621–16631 (2023) 4
3. Chen, Z., Funkhouser, T., Hedman, P., Tagliasacchi, A.: Mobilenerf: Exploiting the polygon rasterization pipeline for efficient neural field rendering on mobile architectures. In: Proceedings of the IEEE/CVF Conference on Computer Vision and Pattern Recognition. pp. 16569–16578 (2023) 4

4. Feng, Y., Feng, X., Shang, Y., Jiang, Y., Yu, C., Zong, Z., Shao, T., Wu, H., Zhou, K., Jiang, C., et al.: Gaussian splashing: Dynamic fluid synthesis with gaussian splatting. arXiv preprint arXiv:2401.15318 (2024) [5](#)
5. Gao, J., Gu, C., Lin, Y., Zhu, H., Cao, X., Zhang, L., Yao, Y.: Relightable 3d gaussian: Real-time point cloud relighting with brdf decomposition and ray tracing. arXiv preprint arXiv:2311.16043 (2023) [7](#)
6. Gao, L., Yang, J., Zhang, B.T., Sun, J.M., Yuan, Y.J., Fu, H., Lai, Y.K.: Mesh-based gaussian splatting for real-time large-scale deformation. arXiv preprint arXiv:2402.04796 (2024) [3](#)
7. Guédon, A., Lepetit, V.: Sugar: Surface-aligned gaussian splatting for efficient 3d mesh reconstruction and high-quality mesh rendering. arXiv preprint arXiv:2311.12775 (2023) [2](#), [3](#), [5](#), [8](#), [10](#), [11](#), [17](#)
8. Hu, L., Zhang, H., Zhang, Y., Zhou, B., Liu, B., Zhang, S., Nie, L.: Gaussianavatar: Towards realistic human avatar modeling from a single video via animatable 3d gaussians. arXiv preprint arXiv:2312.02134 (2023) [5](#)
9. Huang, Y.H., Sun, Y.T., Yang, Z., Lyu, X., Cao, Y.P., Qi, X.: Sc-gs: Sparse-controlled gaussian splatting for editable dynamic scenes. arXiv preprint arXiv:2312.14937 (2023) [5](#)
10. Jambon, C., Kerbl, B., Kopanas, G., Diolatzis, S., Drettakis, G., Leimkühler, T.: Nerfshop: Interactive editing of neural radiance fields. Proceedings of the ACM on Computer Graphics and Interactive Techniques **6**(1) (2023) [2](#), [4](#)
11. Jensen, R., Dahl, A., Vogiatzis, G., Tola, E., Aanaes, H.: Large scale multi-view stereopsis evaluation. In: Proceedings of the IEEE conference on computer vision and pattern recognition. pp. 406–413 (2014) [10](#), [15](#)
12. Jiang, Y., Yu, C., Xie, T., Li, X., Feng, Y., Wang, H., Li, M., Lau, H., Gao, F., Yang, Y., et al.: Vr-gs: A physical dynamics-aware interactive gaussian splatting system in virtual reality. arXiv preprint arXiv:2401.16663 (2024) [5](#)
13. Kazhdan, M., Hoppe, H.: Screened poisson surface reconstruction. ACM Transactions on Graphics (ToG) **32**(3), 1–13 (2013) [7](#), [15](#)
14. Kerbl, B., Kopanas, G., Leimkühler, T., Drettakis, G.: 3d gaussian splatting for real-time radiance field rendering. ACM Transactions on Graphics **42**(4) (2023) [2](#), [5](#), [6](#), [8](#)
15. Kirschstein, T., Giebenhain, S., Nießner, M.: Diffusionavatars: Deferred diffusion for high-fidelity 3d head avatars. arXiv preprint arXiv:2311.18635 (2023) [5](#)
16. Liang, Z., Zhang, Q., Feng, Y., Shan, Y., Jia, K.: Gs-ir: 3d gaussian splatting for inverse rendering. arXiv preprint arXiv:2311.16473 (2023) [7](#)
17. Lin, Y., Dai, Z., Zhu, S., Yao, Y.: Gaussian-flow: 4d reconstruction with dynamic 3d gaussian particle. arXiv preprint arXiv:2312.03431 (2023) [5](#)
18. Liu, R., Xiang, J., Zhao, B., Zhang, R., Yu, J., Zheng, C.: Neural impostor: Editing neural radiance fields with explicit shape manipulation. In: Computer Graphics Forum. vol. 42, p. e14981. Wiley Online Library (2023) [2](#), [4](#)
19. Liu, S., Zhang, X., Zhang, Z., Zhang, R., Zhu, J.Y., Russell, B.: Editing conditional radiance fields. In: Proceedings of the IEEE/CVF international conference on computer vision. pp. 5773–5783 (2021) [4](#), [10](#), [11](#), [12](#)
20. Ma, L., Li, X., Liao, J., Wang, X., Zhang, Q., Wang, J., Sander, P.V.: Neural parameterization for dynamic human head editing. ACM Transactions on Graphics (TOG) **41**(6), 1–15 (2022) [4](#)
21. Mildenhall, B., Srinivasan, P.P., Tancik, M., Barron, J.T., Ramamoorthi, R., Ng, R.: Nerf: Representing scenes as neural radiance fields for view synthesis. Communications of the ACM **65**(1), 99–106 (2021) [2](#), [4](#), [10](#), [15](#)

22. Qian, S., Kirschstein, T., Schoneveld, L., Davoli, D., Giebenhain, S., Nießner, M.: Gaussianavatars: Photorealistic head avatars with rigged 3d gaussians. arXiv preprint arXiv:2312.02069 (2023) [5](#)
23. Radford, A., Kim, J.W., Hallacy, C., Ramesh, A., Goh, G., Agarwal, S., Sastry, G., Askell, A., Mishkin, P., Clark, J., et al.: Learning transferable visual models from natural language supervision. In: International conference on machine learning. pp. 8748–8763. PMLR (2021) [4](#)
24. Rakotosaona, M.J., Manhardt, F., Arroyo, D.M., Niemeyer, M., Kundu, A., Tombari, F.: Nerfmeshing: Distilling neural radiance fields into geometrically-accurate 3d meshes. arXiv preprint arXiv:2303.09431 (2023) [4](#), [5](#)
25. Sun, J., Wang, X., Zhang, Y., Li, X., Zhang, Q., Liu, Y., Wang, J.: Fenerf: Face editing in neural radiance fields. In: Proceedings of the IEEE/CVF Conference on Computer Vision and Pattern Recognition. pp. 7672–7682 (2022) [4](#)
26. Tang, J., Ren, J., Zhou, H., Liu, Z., Zeng, G.: Dreamgaussian: Generative gaussian splatting for efficient 3d content creation. arXiv preprint arXiv:2309.16653 (2023) [7](#)
27. Tang, J., Zhou, H., Chen, X., Hu, T., Ding, E., Wang, J., Zeng, G.: Delicate textured mesh recovery from nerf via adaptive surface refinement. arXiv preprint arXiv:2303.02091 (2023) [4](#)
28. Waczyńska, J., Borycki, P., Tadeja, S., Tabor, J., Spurek, P.: Games: Mesh-based adapting and modification of gaussian splatting. arXiv preprint arXiv:2402.01459 (2024) [3](#)
29. Wang, C., Chai, M., He, M., Chen, D., Liao, J.: Clip-nerf: Text-and-image driven manipulation of neural radiance fields. In: Proceedings of the IEEE/CVF Conference on Computer Vision and Pattern Recognition. pp. 3835–3844 (2022) [4](#)
30. Wang, C., He, M., Chai, M., Chen, D., Liao, J.: Mesh-guided neural implicit field editing. arXiv preprint arXiv:2312.02157 (2023) [4](#)
31. Wang, P., Liu, L., Liu, Y., Theobalt, C., Komura, T., Wang, W.: Neus: Learning neural implicit surfaces by volume rendering for multi-view reconstruction. arXiv preprint arXiv:2106.10689 (2021) [2](#), [7](#), [8](#), [10](#), [15](#), [18](#)
32. Wang, X., Zhu, J., Ye, Q., Huo, Y., Ran, Y., Zhong, Z., Chen, J.: Seal-3d: Interactive pixel-level editing for neural radiance fields (2023) [4](#)
33. Wu, G., Yi, T., Fang, J., Xie, L., Zhang, X., Wei, W., Liu, W., Tian, Q., Wang, X.: 4d gaussian splatting for real-time dynamic scene rendering. arXiv preprint arXiv:2310.08528 (2023) [5](#)
34. Xiang, F., Xu, Z., Hasan, M., Hold-Geoffroy, Y., Sunkavalli, K., Su, H.: Neutex: Neural texture mapping for volumetric neural rendering. In: Proceedings of the IEEE/CVF Conference on Computer Vision and Pattern Recognition. pp. 7119–7128 (2021) [4](#)
35. Xie, T., Zong, Z., Qiu, Y., Li, X., Feng, Y., Yang, Y., Jiang, C.: Physgaussian: Physics-integrated 3d gaussians for generative dynamics. arXiv preprint arXiv:2311.12198 (2023) [5](#)
36. Xu, Q., Xu, Z., Philip, J., Bi, S., Shu, Z., Sunkavalli, K., Neumann, U.: Point-nerf: Point-based neural radiance fields. In: Proceedings of the IEEE/CVF Conference on Computer Vision and Pattern Recognition. pp. 5438–5448 (2022) [2](#)
37. Xu, Y., Chen, B., Li, Z., Zhang, H., Wang, L., Zheng, Z., Liu, Y.: Gaussian head avatar: Ultra high-fidelity head avatar via dynamic gaussians. arXiv preprint arXiv:2312.03029 (2023) [5](#)
38. Yang, B., Bao, C., Zeng, J., Bao, H., Zhang, Y., Cui, Z., Zhang, G.: Neumesh: Learning disentangled neural mesh-based implicit field for geometry and texture

- editing. In: European Conference on Computer Vision. pp. 597–614. Springer (2022) [2](#), [4](#), [18](#)
39. Yang, Z., Gao, X., Zhou, W., Jiao, S., Zhang, Y., Jin, X.: Deformable 3d gaussians for high-fidelity monocular dynamic scene reconstruction. arXiv preprint arXiv:2309.13101 (2023) [5](#)
 40. Yao, Y., Zhang, J., Liu, J., Qu, Y., Fang, T., McKinnon, D., Tsin, Y., Quan, L.: Neif: Neural incident light field for physically-based material estimation. In: European Conference on Computer Vision. pp. 700–716. Springer (2022) [4](#)
 41. Yariv, L., Hedman, P., Reiser, C., Verbin, D., Srinivasan, P.P., Szeliski, R., Barron, J.T., Mildenhall, B.: Baked sdf: Meshing neural sdf for real-time view synthesis. arXiv preprint arXiv:2302.14859 (2023) [4](#), [5](#)
 42. Yuan, Y., Li, X., Huang, Y., De Mello, S., Nagano, K., Kautz, J., Iqbal, U.: Gavatar: Animatable 3d gaussian avatars with implicit mesh learning. arXiv preprint arXiv:2312.11461 (2023) [5](#)
 43. Yuan, Y.J., Sun, Y.T., Lai, Y.K., Ma, Y., Jia, R., Gao, L.: Nerf-editing: geometry editing of neural radiance fields. In: Proceedings of the IEEE/CVF Conference on Computer Vision and Pattern Recognition. pp. 18353–18364 (2022) [2](#), [4](#)
 44. Zhan, F., Liu, L., Kortylewski, A., Theobalt, C.: General neural gauge fields. arXiv preprint arXiv:2305.03462 (2023) [4](#)
 45. Zhang, J., Li, X., Wan, Z., Wang, C., Liao, J.: Fdnerf: Few-shot dynamic neural radiance fields for face reconstruction and expression editing. In: SIGGRAPH Asia 2022 Conference Papers. pp. 1–9 (2022) [4](#)
 46. Zheng, Z., Huang, H., Yu, T., Zhang, H., Guo, Y., Liu, Y.: Structured local radiance fields for human avatar modeling. In: Proceedings of the IEEE/CVF Conference on Computer Vision and Pattern Recognition. pp. 15893–15903 (2022) [4](#)
 47. Zhou, K., Hong, L., Xie, E., Yang, Y., Li, Z., Zhang, W.: Serf: Fine-grained interactive 3d segmentation and editing with radiance fields. arXiv preprint arXiv:2312.15856 (2023) [2](#), [4](#)
 48. Zhou, X., Lin, Z., Shan, X., Wang, Y., Sun, D., Yang, M.H.: Drivinggaussian: Composite gaussian splatting for surrounding dynamic autonomous driving scenes. arXiv preprint arXiv:2312.07920 (2023) [5](#)
 49. Zielonka, W., Bagautdinov, T., Saito, S., Zollhöfer, M., Thies, J., Romero, J.: Drivable 3d gaussian avatars. arXiv preprint arXiv:2311.08581 (2023) [5](#)
 50. Zwicker, M., Pfister, H., Van Baar, J., Gross, M.: Ewa splatting. IEEE Transactions on Visualization and Computer Graphics **8**(3), 223–238 (2002) [6](#)